Formation Flying for Electric Sails in Displaced Orbits.
Part II: Distributed Coordinated Control

Wei Wang[(1)], Giovanni Mengali[(2)]*, Alessandro A. Quarta[(2)], Jianping Yuan[(1)]

[(1)] *National Key Laboratory of Aerospace of Flight Dynamics, Northwestern Polytechnical University, 710072 Xi'an, People's Republic of China*

[(2)] *Dipartimento di Ingegneria Civile e Industriale, University of Pisa, I-56122 Pisa, Italy*

Abstract

We analyze a cooperative control framework for electric sail formation flying around a heliocentric displaced orbit, aiming at observing the polar region of a celestial body. The chief spacecraft is assumed to move along an elliptic displaced orbit, while each deputy spacecraft adjusts its thrust vector (that is, both its sail attitude and characteristic acceleration) in order to track a prescribed relative trajectory. The relative motion of the electric sail formation system is formulated in the chief rotating frame, where the control inputs of each deputy are the relative sail attitude angles and the relative lightness number with respect to those of the chief. The information exchange among the spacecraft, characterized by the communication topology, is represented by a weighted graph. Two typical cases, according to whether the communication graph is directed or undirected, are discussed. For each case, a distributed coordinated control law is designed in such a way that each deputy not only tracks the chief state, but also makes full use of information from its neighbours, thus increasing the redundancy and robustness of the formation system in case of failure between the communication links. Illustrative examples show the effectiveness of the proposed approach.

Keywords: Electric solar wind sail, Displaced orbit, Formation flying, Distributed control

Nomenclature

a	=	orbital semimajor axis, [au]
$a_\oplus$	=	spacecraft characteristic acceleration, [mm/s^2]
$\boldsymbol{a}$	=	propulsive acceleration, [mm/s^2]
B	=	celestial body
e	=	orbital eccentricity
$\boldsymbol{e}$	=	relative position errors [m]
$\mathcal{E}$	=	set of edges
f	=	true anomaly, [rad]
$\mathcal{G}$	=	communication topology graph
H	=	displacement, [au]
I	=	identity matrix
$\mathcal{L}$	=	Laplacian matrix (with entries $[l_{ij}]$)
N	=	number of deputy spacecraft

*Corresponding author

Email addresses: 418362467@qq.com (Wei Wang[(1)]), g.mengali@ing.unipi.it (Giovanni Mengali[(2)]), a.quarta@ing.unipi.it (Alessandro A. Quarta[(2)]), jyuan@nwpu.edu.cn (Jianping Yuan[(1)])

n	=	mean motion of displaced orbit, [rad/day]
n_r	=	angular velocity of reference relative orbit, [rad/day]
O	=	Sun's center-of-mass
o	=	focus of displaced orbit
$\boldsymbol{q}$	=	auxiliary vector
R	=	focus-spacecraft distance [au]
$\boldsymbol{r}$	=	position vector (with $r = \|\boldsymbol{r}\|$), [au]
S	=	spacecraft
t	=	time, [days]
$\mathcal{T}_I$	=	inertial reference frame
$\mathcal{T}_R$	=	rotating reference frame
$\boldsymbol{u}$	=	control input of deputy
$\mathcal{V}$	=	set of vertices
$\hat{\boldsymbol{x}}, \hat{\boldsymbol{y}}, \hat{\boldsymbol{z}}$	=	unit vectors of coordinate axes
$\mathcal{W}$	=	weighted adjacency matrix (with entries $[w_{ij}]$)
α	=	cone angle, [rad]
β	=	lightness number
γ	=	elevation angle, [rad]
θ, φ	=	attitude angles, [rad]
κ	=	dimensionless propulsive acceleration
$\mu_\odot$	=	Sun's gravitational parameter, [au^3/day^2]
ρ_x, ρ_y, ρ_z	=	components of relative position vector in chief's rotating frame, [km]
$\boldsymbol{\rho}$	=	relative position vector, [km]
υ	=	vertex
$\boldsymbol{\omega}$	=	angular velocity vector (with $\omega = \|\boldsymbol{\omega}\|$), [rad/s]

Subscripts

B	=	celestial body
C	=	chief
i	=	i-th deputy
max	=	maximum
S	=	spacecraft
$\odot$	=	Sun

Superscripts

T	=	transpose
$\star$	=	reference value
$\cdot$	=	time derivative
$\wedge$	=	unit vector

1. Introduction

In recent years, much effort has been devoted to the study of an Electric Solar Wind Sail (E-sail), an interesting propulsion system that uses the natural solar wind dynamic pressure to generate a continuous low-thrust, without the need of any reaction mass [7, 10, 18]. A potential and challenging mission scenario of an E-sail-based spacecraft is to generate a heliocentric closed trajectory, usually referred to as displaced orbit [9, 5, 16], in which the continuous propulsive acceleration is used to shift the spacecraft orbital plane off the Sun's center-of-mass. A scientific application of this unusual trajectory is, for example, to continuously observe the polar region of a celestial body, such as a planet or an asteroid. However, the propulsive requirements for this kind of mission scenario, given in terms of maximum value of propulsive acceleration necessary to maintain the displaced orbit, could be beyond the technological capabilities of an E-sail propulsion system.

A possible solution to this problem is to reduce the spacecraft launch mass (with a subsequent increase of the E-sail characteristic acceleration) by distributing the payload among different E-sail-based vehicles operating in a formation flight, where each functional module (spacecraft) of the formation takes the essential mass only [8, 17].

So far, the control problem of different spacecraft flying around a heliocentric displaced orbit falls into two main categories, that is, control with single or leader-follower strategy. In the first case the concept is to distribute a number of sail-based (either photonic solar sail or E-sail) spacecraft into different displaced orbits and to control them separately, without the need of any real-time information about the position of each spacecraft with respect to the chief vehicle [25, 23]. In a companion paper [24] the same idea has been applied to a set of E-sail spacecraft in a formation flight. With such a simple control strategy, some typical formation geometries, as well as the bounds of the spacecraft relative motion, can be analytically estimated by selecting the displaced orbital elements. However, the robustness of the formation system cannot be guaranteed since no stability control is involved.

The second concept, instead, assumes the chief spacecraft to follow a prescribed displaced orbit, and the deputies to adjust their thrust vectors (that is, both the sail attitude and the characteristic acceleration) in order to track the desired relative trajectories with respect to the chief [3, 4]. This is the so called chief-deputy or leader-follower control strategy. Nevertheless, inherent limitations also exist in the latter system arrangement. For example, the unique chief spacecraft, which represents the only information source about the reference state for each deputy, is a single point of massive failure for the whole group [13]. Another weakness associated with a chief-deputy strategy is the absence of a mutual feedback information flow throughout the formation structure. As a result, an unfavorable situation may arise if a fault happens in the chief-deputy communication links. A possible improvement consists in including the information exchange among the deputies into the feedback control. In addition, it has been proved that the mutual connection of agents also contributes to an accuracy enhancement during the transient motion [12].

Recognizing these issues, this paper concentrates on the problem of cooperative control for multiple E-sail formation flight around a heliocentric (elliptic) displaced orbit, by making full use of the measurable information among the formation structure. In particular, two qualitatively different cases involving either a "directed" or an "undirected" weighted graph of communication topology are addressed via consensus algorithms [12]. The basic idea of information consensus is that each agent in a group updates its state on the basis of the data obtained from its local neighbours, in such a way that the final state of each agent converges to some consistent common value. In addition, the fundamental protocol of the consensus algorithm can be extended to deal with the problem that the state of each agent converges to a desired relative separation value or incorporate different group behaviors into the consensus building process [15]. The emphasis of this work relies on the fact that every available neighbour-to-neighbour information exchange among deputy E-sails is included into the feedback control system, thus preventing an undesirable situation in which a failure of the chief spacecraft would give rise to potential risks to the whole formation structure. In this sense, this analysis completes the results of [24] where the chief-deputy relative motion is discussed without the use of a cooperative control.

The paper is organized as follows. The next section briefly summarizes the mathematical model used to calculate the E-sail propulsive requirements necessary to maintain a prescribed heliocentric displaced orbit. In particular, with the aid of the main results discussed in [24], section 2 illustrates the model for analyzing the relative motion of two spacecraft around a heliocentric, elliptic, displaced orbit. This relative dynamics is then used in section 3 for the study of the control system. The latter, which is based on the consensus algorithm, allows the E-sail thrust vector to be oriented so as to track the desired chief-deputy relative trajectory. The control system effectiveness is then investigated in section 4 by means of numerical simulation of some mission scenarios of particular interest. Finally, section 5 contains the concluding remarks.

2. E-sail relative motion around an elliptic displaced orbit

Consider a mission scenario in which a chief spacecraft tracks a heliocentric elliptic displaced orbit while some deputy spacecraft are controlled to operate around the chief. The characteristics of the displaced orbit and the spacecraft control law are selected in order to ensure that the vehicles (closely) follow the heliocentric trajectory of a reference celestial body B with an eccentricity $e_B < 1$ and a semimajor axis a_B, as is now discussed.

2.1. Displaced orbit and thrust vector characteristics

Assume that a spacecraft S tracks an elliptic displaced orbit having semimajor axis $a_S \leq a_B$ and eccentricity $e_S < 1$, with a local angular velocity $\boldsymbol{\omega}_S$ that matches the instantaneous angular velocity $\boldsymbol{\omega}_B$ of the reference celestial body B. Introduce the two reference frames illustrated in Fig. 1 to describe the spacecraft motion around the displaced orbit [24]. The first one is a heliocentric inertial reference frame $\mathcal{T}_I(O; \hat{\boldsymbol{x}}_I, \hat{\boldsymbol{y}}_I, \hat{\boldsymbol{z}}_I)$ centered at the Sun's center-of-mass O, where the plane $(\hat{\boldsymbol{x}}_I, \hat{\boldsymbol{y}}_I)$ contains the reference Keplerian orbit, $\hat{\boldsymbol{x}}_I$ points to the perihelion and $\hat{\boldsymbol{z}}_I$ is positive in the direction of the celestial body's angular momentum vector $\boldsymbol{h}_B$. The second one, $\mathcal{T}_R(S; \hat{\boldsymbol{x}}_R, \hat{\boldsymbol{y}}_R, \hat{\boldsymbol{z}}_R)$, is a rotating reference frame centered at the spacecraft center-of-mass. The plane $(\hat{\boldsymbol{x}}_R, \hat{\boldsymbol{y}}_R)$ coincides the displaced orbital plane which is, by assumption, parallel to the plane $(\hat{\boldsymbol{x}}_I, \hat{\boldsymbol{y}}_I)$ and is placed at a given distance H_S from it, see Fig. 1. In particular, $\hat{\boldsymbol{z}}_R \equiv \hat{\boldsymbol{z}}_I$ and the unit vector $\hat{\boldsymbol{x}}_R$ is directed from the displaced orbit's focus o to spacecraft S.
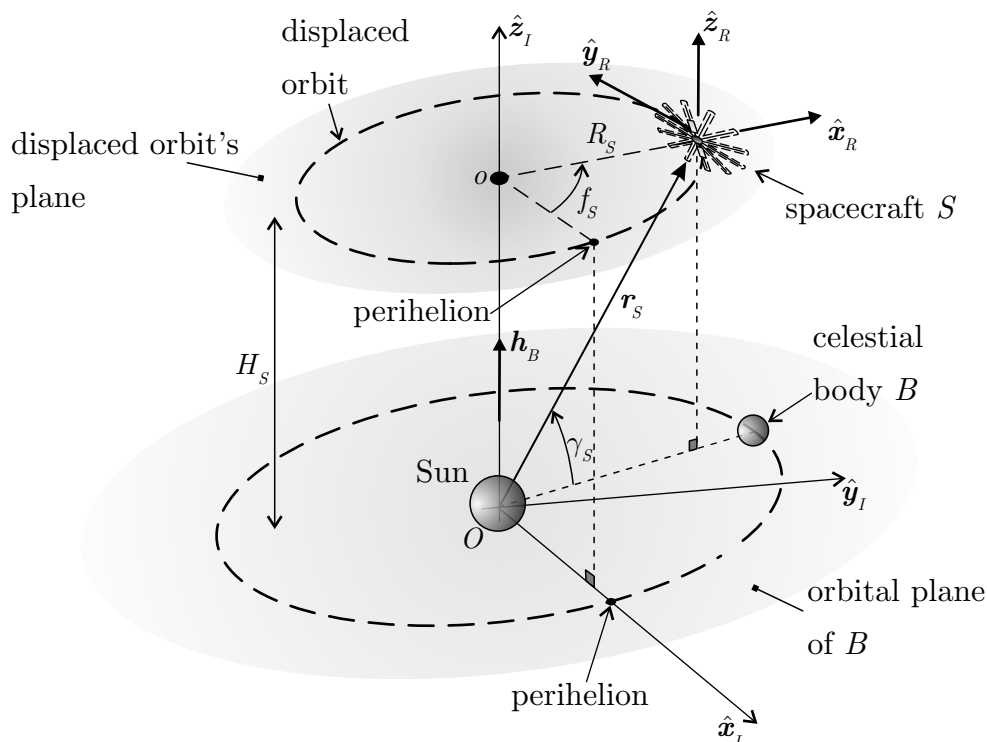

Figure 1: Reference frames (adapted from [24]).

The spacecraft displaced orbit has the following characteristics: 1) the eccentricity is equal to that of the celestial body's orbit (i.e. $e_S = e_B$); 2) the focus o coincides with the orthogonal projection of O onto the plane $(\hat{\boldsymbol{x}}_R, \hat{\boldsymbol{y}}_R)$; 3) the perihelion belongs to the plane $(\hat{\boldsymbol{x}}_I, \hat{\boldsymbol{z}}_I)$. Such a displaced orbit is called a Planet Following Displaced Orbit (PFDO) [11] since, if the chief and the celestial body pass through their pericenter at the same time, the spacecraft and the celestial body belong to a plane containing the unit vector $\hat{\boldsymbol{z}}_I$ at any time instant, see Fig. 1. This orbital arrangement is particularly useful as it guarantees, for example, a continuous observation of the poles of the celestial body.

The propulsive acceleration $\boldsymbol{a}_S$ of an E-sail-based spacecraft can be written as [26, 27]

$$\boldsymbol{a}_S = a_{\oplus_S} \, \kappa_S \left(\frac{r_\oplus}{r_S}\right) \hat{\boldsymbol{a}}_S = \beta \, \frac{\mu_\odot}{r_\oplus^2} \, \kappa_S \left(\frac{r_\oplus}{r_S}\right) \hat{\boldsymbol{a}}_S \tag{1}$$

where r_S is the Sun-spacecraft distance, $a_{\oplus_S}$ is the E-sail characteristic acceleration (that is, the maximum modulus of the propulsive acceleration at a reference distance $r_S = r_\oplus \triangleq 1\,\mathrm{au}$), $\beta_S \triangleq \frac{a_{\oplus_S}}{\mu_\odot / r_\oplus^2}$ is the sail lightness number, and $\kappa_S \leq 1$ is the dimensionless propulsive acceleration [24, 11] whose local value depends

on the E-sail cone angle α_S, defined as the angle between the Sun-spacecraft unit vector $\hat{\boldsymbol{r}}_S$ and the propulsive acceleration unit vector $\hat{\boldsymbol{a}}_S$. The function $\kappa_S = \kappa_S(\alpha_S)$, drawn in Fig. 2, shows that the E-sail cone angle has a maximum value of about $\alpha_{S_{\max}} \triangleq \max(\alpha_S) \simeq 19.7 \, \mathrm{deg}$.
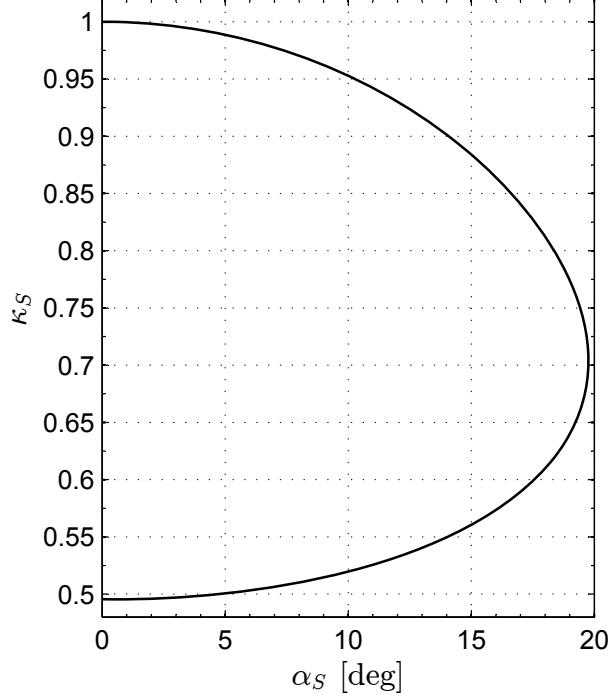

Figure 2: Dimensionless propulsive acceleration κ_S as a function of the E-sail cone angle α_S.

The components of $\hat{\boldsymbol{a}}_S$ in the rotating reference frame $\mathcal{T}_R$ can be written as

$$[\hat{\boldsymbol{a}}_S]_{\mathcal{T}_R} = [\cos\theta_S \, \cos\varphi_S, \, \sin\theta_S, \, \cos\theta_S \, \sin\varphi_S]^{\mathrm{T}} \tag{2}$$

where $\theta_S \in [0, 2\pi]$ is the angle between the $(\hat{\boldsymbol{x}}_R, \hat{\boldsymbol{z}}_R)$ plane and the direction of $\hat{\boldsymbol{a}}_S$, while $\varphi_S \in [0, 2\pi]$ is measured from the $\hat{\boldsymbol{x}}_R$ axis to the projection of $\hat{\boldsymbol{a}}_S$ onto the $(\hat{\boldsymbol{x}}_R, \hat{\boldsymbol{z}}_R)$ plane, see Fig. 3. Note that the value of $a_{\oplus S}$ in Eq. (1) can be slightly modulated by adjusting the E-sail tether voltage [6, 21, 22].

The analytical conditions required for maintaining an elliptic PFDO are [24]

$$\tan\alpha_S = \frac{\tan\gamma_S \, \sqrt{1 + \tan^2\gamma_S}}{(a_B/a_S)^3 - \sqrt{1 + \tan^2\gamma_S}} \tag{3}$$

$$\beta_S = \frac{r_\oplus}{\kappa_S \, H_S} \sqrt{\frac{\tan^2\gamma_S \, (1 + \tan^2\gamma_S)}{(a_B/a_S)^6} - \frac{2\,\tan^2\gamma_S}{(a_B/a_S)^3 \, \sqrt{1 + \tan^2\gamma_S}} + \frac{\tan^2\gamma_S}{1 + \tan^2\gamma_S}} \tag{4}$$

where $\mu_\odot$ is the Sun's gravitational parameter, $\gamma_S \triangleq \arctan(H_S/R_S)$ is the spacecraft elevation angle, and R_S is the focus-spacecraft distance given by

$$R_S = \frac{a_S \, (1 - e_S^2)}{1 + e_S \, \cos f_S} \tag{5}$$

and f_S is the spacecraft true anomaly from the periapsis of the displaced orbit, see Fig. 1.

For an elliptic PFDO, that is, when $e_B \neq 0$, the value of γ_S (and so the required value of α_S and $a_{\oplus S}$) varies along the orbit. In other terms, a PFDO of given characteristics $\{a_S, e_S, H_S\}$ can be maintained by continuously controlling the sail attitude (through the cone angle in accordance with Eq. (3)) and the characteristic acceleration or, equivalently, the sail lightness number β_S, see Eq. (4).
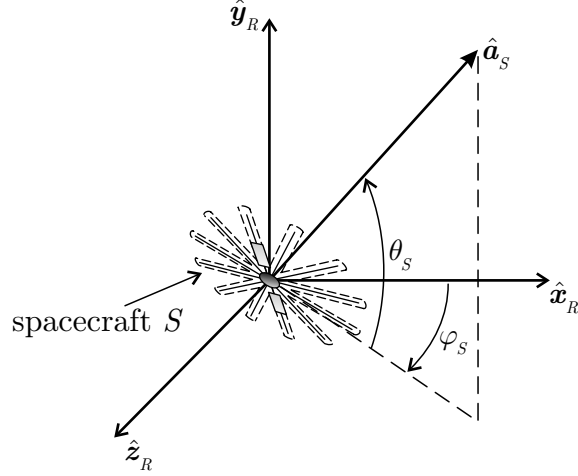
5

Figure 3: Characteristic angles of the E-sail propulsive acceleration vector $\boldsymbol{a}_S$.

2.2. Chief-deputy relative dynamics

Let $\boldsymbol{\rho}_i \triangleq \boldsymbol{r}_i - \boldsymbol{r}_C$ denote the relative position vector between the i-th deputy and the chief spacecraft, with

$$[\boldsymbol{r}_C]_{\mathcal{T}_R} = [R_C, \ 0, \ H_C]^{\mathrm{T}} \tag{6}$$

where the focus-chief distance R_C is given by Eq. (5) as a function of the chief true anomaly f_C on the displaced orbit. The equation of relative motion in the chief rotating reference frame $\mathcal{T}_R$ can be written as

$$\ddot{\boldsymbol{\rho}}_i + 2\,\boldsymbol{\omega}_C \times \dot{\boldsymbol{\rho}}_i + \dot{\boldsymbol{\omega}}_C \times \boldsymbol{\rho}_i + \boldsymbol{\omega}_C \times (\boldsymbol{\omega}_C \times \boldsymbol{\rho}_i) = -\frac{\mu_\odot}{r_i^3}\,\boldsymbol{r}_i + \frac{\mu_\odot}{r_C^3}\,\boldsymbol{r}_C + \boldsymbol{a}_i - \boldsymbol{a}_C \tag{7}$$

where the chief's angular velocity $\boldsymbol{\omega}_C$ is given by

$$[\boldsymbol{\omega}_C]_{\mathcal{T}_R} = [0, \ 0, \ \omega_C]^{\mathrm{T}} \tag{8}$$

with

$$\omega_C = \|\boldsymbol{\omega}_C\| = \frac{n\,(1 + e_C\,\cos f_C)^2}{\sqrt{(1 - e_C^2)^3}} \tag{9}$$

and $n \triangleq \sqrt{\mu_\odot / a_B^3}$ is the mean motion of the celestial body.

Since the relative chief-deputy distance is much smaller than the Sun-chief distance, the propulsive acceleration $(\boldsymbol{a}_i)$ and the gravitational acceleration $(-\mu_\odot\,\boldsymbol{r}_i/r_i^3)$ of the i-th deputy can be linearized around those of the chief, viz.

$$\boldsymbol{a}_i \simeq \boldsymbol{a}_C + \frac{\partial \boldsymbol{a}_C}{\partial \boldsymbol{r}_C}\,\boldsymbol{\rho}_i + \frac{\partial \boldsymbol{a}_C}{\partial \beta_C}\,\Delta\beta_i + \frac{\partial \boldsymbol{a}_C}{\partial \hat{\boldsymbol{a}}_C}\,\Delta\hat{\boldsymbol{a}}_i \tag{10}$$

$$-\frac{\mu_\odot}{r_i^3}\,\boldsymbol{r}_i \simeq -\frac{\mu_\odot}{r_C^3}\,\boldsymbol{r}_C + \frac{\partial(-\mu_\odot\,\boldsymbol{r_C}/r_C^3)}{\partial \boldsymbol{r}_C}\,\boldsymbol{\rho}_i \tag{11}$$

6

where $\Delta \beta_i \triangleq \beta_i - \beta_C$ is the relative lightness number, $\Delta \hat{\boldsymbol{a}}_i \triangleq \hat{\boldsymbol{a}}_i - \hat{\boldsymbol{a}}_C$ is the relative unit thrust vector, and

$$\frac{\partial \boldsymbol{a}_C}{\partial \boldsymbol{r}_C} = -\frac{\beta_C \, \kappa_C \, \mu_\odot}{r_\oplus \, r_C^3} \, \hat{\boldsymbol{a}}_C \, \boldsymbol{r}_C^{\mathrm{T}} \tag{12}$$

$$\frac{\partial \boldsymbol{a}_C}{\partial \beta_C} = \frac{\kappa_C \, \mu_\odot}{r_\oplus \, r_C} \, \hat{\boldsymbol{a}}_C \tag{13}$$

$$\frac{\partial \boldsymbol{a}_C}{\partial \hat{\boldsymbol{a}}_C} = \frac{\beta_C \, \kappa_C \, \mu_\odot}{r_\oplus \, r_C} \, I_3 \tag{14}$$

$$\frac{\partial (-\mu_\odot \, \boldsymbol{r}_C / r_C^3)}{\partial \boldsymbol{r}_C} = \frac{3 \, \mu_\odot}{r_C^5} \, \boldsymbol{r}_C \, \boldsymbol{r}_C^{\mathrm{T}} - \frac{\mu_\odot}{r_C^3} \, I_3 \tag{15}$$

where I_3 is the 3×3 identity matrix.

Strictly speaking, Eq. (10) should also account for the variation of the chief dimensionless propulsive acceleration κ_C, which is a function of the chief cone angle α_C [26, 27]. However, for a heliocentric displaced orbit with a small eccentricity, the parameter κ_C varies within a very small range. For example, assuming an Earth-synchronous elliptic displaced orbit with a semimajor axis $a_C = 0.95$ au and a displacement $H_C = 0.05$ au, κ_C oscillates periodically with a maximum variation of about 10^{-2} around a mean value of 0.82. Using the mean value of κ_C in the simulations, the maximum induced error is less than 0.7%. Accordingly, in what follows the dimensionless propulsive acceleration κ_C is assumed to be constant in differentiation operation.

Since $\hat{\boldsymbol{a}}_i$ is a function of the i-th deputy thrust angles, see Eq. (2), it can be further linearized as

$$\Delta \hat{\boldsymbol{a}}_i \simeq \frac{\partial \hat{\boldsymbol{a}}_C}{\partial [\varphi_C, \, \theta_C]} \, [\Delta \varphi_i, \, \Delta \theta_i]^{\mathrm{T}} \tag{16}$$

where the Jacobian matrix is

$$\frac{\partial \hat{\boldsymbol{a}}_C}{\partial [\varphi_C, \, \theta_C]} = \begin{bmatrix} -\sin \varphi_C \, \cos \theta_C & -\cos \varphi_C \, \sin \theta_C \\ 0 & \cos \theta_C \\ \cos \varphi_C \, \cos \theta_C & -\sin \varphi_C \, \sin \theta_C \end{bmatrix} \tag{17}$$

while $\Delta \varphi_i \triangleq \varphi_i - \varphi_C$ and $\Delta \theta_i \triangleq \theta_i - \theta_C$ are the relative E-sail thrust angles between the i-th deputy and the chief spacecraft. In particular, since the chief tracks an elliptic PFDO, $\theta_C = 0$ and $\varphi_C = \alpha_C + \gamma_C$. Substituting Eqs. (8)–(17) into Eq. (7), the differential equation of the chief-deputy relative motion becomes

$$\ddot{\boldsymbol{\rho}}_i + 2 \, W \, \dot{\boldsymbol{\rho}}_i + P \, \boldsymbol{\rho}_i = C \, \boldsymbol{u}_i \tag{18}$$

where $\boldsymbol{u}_i$ is the control input of the i-th deputy sail, defined as

$$\boldsymbol{u}_i = [\Delta \varphi_i, \, \Delta \theta_i, \, \Delta \beta_i]^{\mathrm{T}} \tag{19}$$

whereas the coefficient matrices W, P and C are given by

$$W = \begin{bmatrix} 0 & -\omega_C & 0 \\ \omega_C & 0 & 0 \\ 0 & 0 & 0 \end{bmatrix} \tag{20}$$

$$P = \begin{bmatrix} -\omega_C^2 + \dfrac{\mu_\odot}{r_C^3} \left(\dfrac{\beta_C \, \kappa_C \, R_C \, \cos \varphi_C}{r_\oplus} - \dfrac{2 \, R_C^2 - H_C^2}{r_C^2} \right) & -\dot{\omega}_C & \dfrac{\mu_\odot}{r_C^3} \left(\dfrac{\beta_C \, \kappa_C \, H_C \, \cos \varphi_C}{r_\oplus} - \dfrac{3 \, R_C \, H_C}{r_C^2} \right) \\ \dot{\omega}_C & \dfrac{\mu_\odot}{r_C^3} - \omega_C^2 & 0 \\ \dfrac{\mu_\odot}{r_C^3} \left(\dfrac{\beta_C \, \kappa_C \, R_C \, \sin \varphi_C}{r_\oplus} - \dfrac{3 \, R_C \, H_C}{r_C^2} \right) & 0 & \dfrac{\mu_\odot}{r_C^3} \left(\dfrac{\beta_C \, \kappa_C \, H_C \, \sin \varphi_C}{r_\oplus} - \dfrac{2 \, H_C^2 - R_C^2}{r_C^2} \right) \end{bmatrix} \tag{21}$$

$$C = \frac{\kappa_C\,\mu_\odot}{r_\oplus\,r_C} \begin{bmatrix} -\beta_C\,\sin\,\varphi_C & 0 & \cos\,\varphi_C \\ 0 & \beta_C & 0 \\ \beta_C\,\cos\,\varphi_C & 0 & \sin\,\varphi_C \end{bmatrix} \tag{22}$$

where, bearing in mind Eq. (9), the angular acceleration of the chief spacecraft is given by

$$\dot{\omega}_C = \frac{-2\,e_C\,n^2\,(1 + e_C\,\cos f_C)^3\,\sin\,f_C}{(1 - e_C^2)^3} \tag{23}$$

Traditional formation flying usually requires an accurate relative geometry maintenance with respect to the chief, whereas some emerging missions, such as spacecraft swarm or cluster flight, only require a bounded separation between deputies. In the analysis to follow, distributed cooperative algorithms involving the formation system described by Eq. (18) will be designed in different mission scenarios, such that all of the deputy spacecraft reach consensus as $t \to +\infty$. In particular, the formation control system is designed to drive each deputy toward a desired trajectory relative to the chief by adjusting both its thrust orientation and the sail lightness number, as is discussed in the next section.

3. Distributed coordinated control

In this section, the formation control of an E-sail-based system consisting of a chief and $N \geq 2$ deputy spacecraft around an elliptic PFDO is considered. Distributed coordinated control laws are developed for both the undirected and directed cases. In particular, the relative motion topology will be represented by an undirected or a directed graph to characterize the information exchange among the formation system.

3.1. Elementary graph theory

To proceed, first introduce some pertinent concepts and notations taken from graph theory [20]. A triplet $\mathcal{G} = (\mathcal{V}, \mathcal{E}, \mathcal{W})$ is a weighted graph with a number of vertices N, where $\mathcal{V}$ is a finite non-empty set of vertices, $\mathcal{E} = \{(v_1, v_2), \ldots, (v_{N-1}, v_N)\} \subseteq \mathcal{V} \times \mathcal{V}$ denotes the set of edges (each edge is a pair of vertices), and $\mathcal{W} = [w_{ij}] \in \mathbb{R}^{N \times N}$ is the weighted adjacency matrix. A path in a graph is a finite or infinite sequence of edges that connect a sequence of vertices. In an undirected graph, an edge $(v_i, v_j) \in \mathcal{E}$ implies a bidirectional path and the mutual transmission of information between vertex v_i and v_j. An undirected graph is called connected if there exists a path between any distinct pair of vertices. On the contrary, in a directed graph (or digraph) an edge $(v_i, v_j) \in \mathcal{E}$ implies that the information flows from vertex v_i to v_j, but not necessarily vice versa. A directed graph is called strongly connected if there is a directed path from every vertex to every other vertex.

The weighted adjacency matrix $\mathcal{W}$ of a graph is a matrix whose generic entry is $w_{ij} > 0 \; \forall \; (v_i, v_j) \in \mathcal{E}$ with $i \neq j$, and $w_{ii} = 0$. In an undirected graph, $\mathcal{W}$ is symmetric because $w_{ij} = w_{ji}$, which is an important property in constructing stable feedback control via consensus algorithm. However, the symmetry property does not hold, in general, for a directed graph. The Laplacian matrix $\mathcal{L} = [l_{ij}] \in \mathbb{R}^{N \times N}$ of a graph $\mathcal{G}$ is defined as $\mathcal{L} \triangleq \mathcal{D} - \mathcal{W}$, where $\mathcal{D} = \mathrm{diag}\,[d_1, \ldots, d_N]$ and $d_i = \sum_{j=1}^{N} w_{ij}$. Note that matrix $\mathcal{L}$ is symmetric positive semi-definite for the undirected case and satisfies $l_{ij} < 0$ and $\sum_{j=1}^{N} l_{ij} = 0, \forall\, i \neq j$. Finally, the topology is assumed to be fixed throughout the paper and the Laplacian matrix $\mathcal{L}$ is constant.

In the topology model of the formation system, each deputy is represented by a vertex, and the information flow between any two vertices is characterized by a weighted edge associated with the pair. Also, it is assumed that each deputy has access to the information from both its neighbours and the chief.

3.2. Undirected topology graph

Consider first the case in which the communication graph $\mathcal{G}$ is undirected and connected. A scenario consisting in maintaining a desired formation shape is analyzed, while the system center position is left free. Such a degree of freedom is typical, for example, of spacecraft swarm (or cluster flight) where a prescribed deputy orientation with respect to the chief (or an inertial frame) is not required. Within these missions,

the center of the formation relative to the chief is determined by the deputies (which is independent of the chief), and the formation flight is said to follow a behavior approach [2].

Let $\boldsymbol{\rho}_i^\star \in \mathbb{R}^3$, with $i = 1, \ldots, N$, characterize the desired (relative) reference position of the i-th deputy E-sail, and introduce the vectors $\boldsymbol{q}_i \triangleq \boldsymbol{\rho}_i - \boldsymbol{\rho}_i^\star$ and $\dot{\boldsymbol{q}}_i \triangleq \dot{\boldsymbol{\rho}}_i - \dot{\boldsymbol{\rho}}_i^\star$. The distributed control law for the system represented by Eq. (18) is chosen as

$$\boldsymbol{u}_i = C^{-1} \left\{ \ddot{\boldsymbol{\rho}}_i^\star + 2\,W\,\dot{\boldsymbol{\rho}}_i^\star + P\,\boldsymbol{\rho}_i - K_i\,\dot{\boldsymbol{q}}_i - \xi \sum_{j=1}^{N} w_{ij} \left[(\boldsymbol{q}_i - \boldsymbol{q}_j) + \zeta\,(\dot{\boldsymbol{q}}_i - \dot{\boldsymbol{q}}_j) \right] \right\} \tag{24}$$

where $K_i \in \mathbb{R}^{3 \times 3}$ and $K_i \in \mathbb{R}^+$, w_{ij} is the (i,j) entry of the weighted adjacency matrix $\mathcal{W}$, $\{\xi, \zeta\} \in \mathbb{R}^+$, while matrices W, P, and C are defined by Eqs. (20)–(22). In particular, it can be verified that C is nonsingular as long as $\beta_C \neq 0$. Note that, unlike the algorithm developed for the chiefless (leaderless) group [14], the control law adopted here allows a reference formation topology to be defined. The following main result is now stated.

Theorem 1: Consider the system described by Eq. (18) with the control law (24). Consensus, that is, $\boldsymbol{q}_i \to \boldsymbol{q}_j$ and $\dot{\boldsymbol{q}}_i \to \boldsymbol{0}$, is guaranteed asymptotically as $t \to +\infty$ if $\mathcal{G}$ is an undirected and connected graph.

Proof: To simplify the subsequent analysis, introduce the compact notation $\boldsymbol{q} \triangleq [\boldsymbol{q}_1^{\mathrm{T}}, \ldots, \boldsymbol{q}_N^{\mathrm{T}}]^{\mathrm{T}}$, $\boldsymbol{u} \triangleq [\boldsymbol{u}_1^{\mathrm{T}}, \ldots, \boldsymbol{u}_N^{\mathrm{T}}]^{\mathrm{T}}$ and $K \triangleq \mathrm{diag}\,\{K_1, \ldots, K_N\}$. Using the control law (24), Eq. (18) can be written as

$$\ddot{\boldsymbol{q}} + [2\,(I_3 \otimes W) + \xi\,\zeta\,(\mathcal{L} \otimes I_3) + K]\,\dot{\boldsymbol{q}} + \xi\,(\mathcal{L} \otimes I_3)\,\boldsymbol{q} = \boldsymbol{0} \tag{25}$$

where $\otimes$ denotes the Kronecker product, and $(\mathcal{L} \otimes I_3)\,\boldsymbol{q}$ is the column stack vector of $\sum_{j=1}^{N} w_{ij}\,(\boldsymbol{q}_i - \boldsymbol{q}_j)$.

Consider the candidate Lyapunov function for Eq. (25) given by

$$V = \frac{1}{2}\,\boldsymbol{q}^{\mathrm{T}}\,(\mathcal{L} \otimes I_3)\,\boldsymbol{q} + \frac{1}{2}\,\dot{\boldsymbol{q}}^{\mathrm{T}}\,\dot{\boldsymbol{q}} \tag{26}$$

Since $\boldsymbol{q}^{\mathrm{T}}\,(\mathcal{L} \otimes I_3)\,\boldsymbol{q} = \frac{1}{2} \sum_{i=1}^{N} \sum_{j=1}^{N} l_{ij} \left\| \boldsymbol{q}_i - \boldsymbol{q}_j \right\|^2 \geq 0$, it follows that V is symmetric positive definite and its time derivative is

$$\dot{V} = -\dot{\boldsymbol{q}}^{\mathrm{T}} K\,\dot{\boldsymbol{q}} - \xi\,\zeta\,\dot{\boldsymbol{q}}^{\mathrm{T}}\,(\mathcal{L} \otimes I_3)\,\dot{\boldsymbol{q}} - 2\,\dot{\boldsymbol{q}}^{\mathrm{T}}\,(I_3 \otimes W)\,\dot{\boldsymbol{q}} \tag{27}$$

According to Eq. (20), matrix W is skew symmetric, therefore, the last term in Eq. (27) is equal to zero. Note that the matrix K is symmetric positive definite, so that

$$\dot{V} = -\dot{\boldsymbol{q}}^{\mathrm{T}} K\,\dot{\boldsymbol{q}} - \xi\,\zeta\,\dot{\boldsymbol{q}}^{\mathrm{T}}\,(\mathcal{L} \otimes I_3)\,\dot{\boldsymbol{q}} \leq 0 \tag{28}$$

For convergence analysis, consider now the second derivative of V. Since $(\mathcal{L} \otimes I_3)\,\boldsymbol{q}$ is the column stack vector of $\sum_{j=1}^{N} w_{ij}\,(\boldsymbol{q}_i - \boldsymbol{q}_j)$, it follows that $(\mathcal{L} \otimes I_3)\,\boldsymbol{q}$ is bounded. Also, since matrices W, K and $\mathcal{L}$ are all bounded, it can be verified from Eq. (25) that $\ddot{\boldsymbol{q}}$ is bounded, hence

$$\left| \ddot{V} \right| \leq 2\,[|\dot{\boldsymbol{q}}^{\mathrm{T}} K\,\ddot{\boldsymbol{q}}| + \xi\,\zeta\,|\dot{\boldsymbol{q}}^{\mathrm{T}}\,(\mathcal{L} \otimes I_3)\,\ddot{\boldsymbol{q}}|] \leq 2\,\|\dot{\boldsymbol{q}}\|\,\|[K + \xi\,\zeta\,(\mathcal{L} \otimes I_3)]\,\ddot{\boldsymbol{q}}\| \tag{29}$$

Equation (29) states that $\ddot{V}$ is also bounded and therefore $\dot{V}$ is uniformly continuous. According to the Barbalat's lemma [19], $\dot{V} \to 0$ as $t \to +\infty$, which further leads to $\dot{\boldsymbol{q}} \to \boldsymbol{0}$. Moreover, it can be drawn from Eq. (25) that $\dddot{\boldsymbol{q}}$ is bounded, therefore $\ddot{\boldsymbol{q}}$ is uniformly continuous. Using the Barbalat's lemma again, $\ddot{\boldsymbol{q}} \to \boldsymbol{0}$ as $t \to +\infty$. Finally, from Eq. (25), it follows that $(\mathcal{L} \otimes I_3)\,\boldsymbol{q} \to \boldsymbol{0}$ as $t \to +\infty$, which amounts to stating that $\boldsymbol{q}_i \to \boldsymbol{q}_j$. This completes the proof.

From the definition of $\boldsymbol{q}_i$, **Theorem 1** further indicates that $(\boldsymbol{\rho}_i - \boldsymbol{\rho}_j) \to (\boldsymbol{\rho}_i^\star - \boldsymbol{\rho}_j^\star)$. Therefore, $\boldsymbol{\rho}_i^\star$ and $\boldsymbol{\rho}_j^\star$ can be chosen so as to acquire a desired separation between the i-th and j-th deputy E-sail.

3.3. Directed topology graph

Unlike the undirected case, the vertices in a directed network are ordered and paths are directed. In particular, the mission considered here consists in tracking a desired relative trajectory $(\boldsymbol{\rho}_i^\star, \dot{\boldsymbol{\rho}}_i^\star) \in \mathbb{R}^3 \times \mathbb{R}^3$. For convenience, let $\boldsymbol{e}_i \triangleq \boldsymbol{\rho}_i - \boldsymbol{\rho}_i^\star$ and $\dot{\boldsymbol{e}}_i \triangleq \dot{\boldsymbol{\rho}}_i - \dot{\boldsymbol{\rho}}_i^\star$ be the position and velocity error of the i-th deputy spacecraft. The aim of the proposed control law is to drive $\boldsymbol{e}_i \to \boldsymbol{0}$ and $\dot{\boldsymbol{e}}_i \to \boldsymbol{0}$, while using information coupling among the deputy E-sails so as to guarantee consensus. In this case the Laplacian matrix $\mathcal{L}$ is (in general) asymmetric, and thus it is difficult to find a Lyapunov function suitable for stability analysis. Therefore, the convergence performance of consensus protocol on a directed graph is a more challenging problem than that for the undirected graph discussed in the previous section.

Paralleling the approach of [14], the second-order consensus protocol is now designed as

$$
\boldsymbol{u}_i = C^{-1} \left\{ \ddot{\boldsymbol{\rho}}_i^\star + 2W\dot{\boldsymbol{\rho}}_i + P\boldsymbol{\rho}_i - \sigma\,(\boldsymbol{e}_i + \zeta\,\dot{\boldsymbol{e}}_i) - \sum_{j=1}^{N} w_{ij}\,[(\boldsymbol{e}_i - \boldsymbol{e}_j) + \zeta\,(\dot{\boldsymbol{e}}_i - \dot{\boldsymbol{e}}_j)] \right\}
\tag{30}
$$

where $\{\sigma, \zeta\} \in \mathbb{R}^+$. Using the control input of Eq. (30) and bearing in mind the differential equation of the chief-deputy relative motion given by Eq. (18), the second-order differential equation for the position error $\boldsymbol{e}_i$ can be written as

$$
\ddot{\boldsymbol{e}}_i + \sigma\,(\boldsymbol{e}_i + \zeta\,\dot{\boldsymbol{e}}_i) + \sum_{j=1}^{N} w_{ij}\,[(\boldsymbol{e}_i - \boldsymbol{e}_j) + \zeta\,(\dot{\boldsymbol{e}}_i - \dot{\boldsymbol{e}}_j)] = \boldsymbol{0}
\tag{31}
$$

A compact form of the previous equation can be obtained by introducing the auxiliary vector $\boldsymbol{e} \triangleq [\boldsymbol{e}_1^{\mathrm{T}}, \ldots, \boldsymbol{e}_N^{\mathrm{T}}]^{\mathrm{T}}$, so that Eq. (31) is rewritten as

$$
[\dot{\boldsymbol{e}}^{\mathrm{T}}, \ddot{\boldsymbol{e}}^{\mathrm{T}}]^{\mathrm{T}} = (\Gamma \otimes I_3)\,[\boldsymbol{e}^{\mathrm{T}}, \dot{\boldsymbol{e}}^{\mathrm{T}}]^{\mathrm{T}}
\tag{32}
$$

where matrix $\Gamma \in \mathbb{R}^{2N \times 2N}$ is defined as

$$
\Gamma \triangleq \begin{bmatrix} \boldsymbol{0}_{N \times N} & I_N \\ -(\sigma\,I_N + \mathcal{L}) & -\zeta\,(\sigma\,I_N + \mathcal{L}) \end{bmatrix}
\tag{33}
$$

The necessary and sufficient stability condition for the linear system of Eq. (33) is that every eigenvalue η_i of Γ has a negative real part. Let λ_i be the i-th eigenvalue of $-(\sigma\,I_N + \mathcal{L})$, it can be shown that

$$
\eta_{i\pm} = \frac{\zeta\,\lambda_i \pm \sqrt{\zeta^2\,\lambda_i^2 + 4\,\lambda_i}}{2}
\tag{34}
$$

Therefore, all of eigenvalues of Γ have negative real parts and the system is asymptotically stable if [13]

$$
\zeta > \max_{i=1,\ldots,N} \sqrt{\frac{2}{|\lambda_i|\cos\left(\dfrac{\pi}{2} - \arctan\dfrac{-\operatorname{Re}(\lambda_i)}{\operatorname{Im}(\lambda_i)}\right)}}
\tag{35}
$$

where $\operatorname{Re}(\cdot)$ and $\operatorname{Im}(\cdot)$ denote the real and imaginary parts of a number, respectively. In particular, to guarantee consensus, that is, $\boldsymbol{e}_i \to \boldsymbol{e}_j \to \boldsymbol{0}$ and $\dot{\boldsymbol{e}}_i \to \dot{\boldsymbol{e}}_j \to \boldsymbol{0}$, a spanning tree must be involved in the topology graph [15], otherwise the relative motion geometry cannot be maintained during the transition even if all of the E-sail-based spacecraft eventually track the reference (desired) formation.

4. Numerical simulations

To illustrate the performance of the proposed consensus-based controllers, a mission scenario involving four E-sail-based spacecraft (one chief and three surrounding deputies, i.e. $i = \{1, 2, 3\}$) is investigated. Using the same example discussed in [24], the chief is assumed to cover an Earth-synchronized elliptic PFDO with its semimajor axis $a_C = 0.95$ au, eccentricity $e_C = e_B = 0.0167$ and displacement $H_C = 0.05$ au. According to Eqs. (3)-(4), the variation of $\{a_{\oplus C}, \alpha_C, \kappa_C\}$ with the true anomaly f_C is shown in Fig. 4. Note that, during a single revolution, the chief (required) characteristic acceleration varies less than 3% around a mean value of about $1.13\,\mathrm{mm/s^2}$, with a maximum of $1.16\,\mathrm{mm/s^2}$.
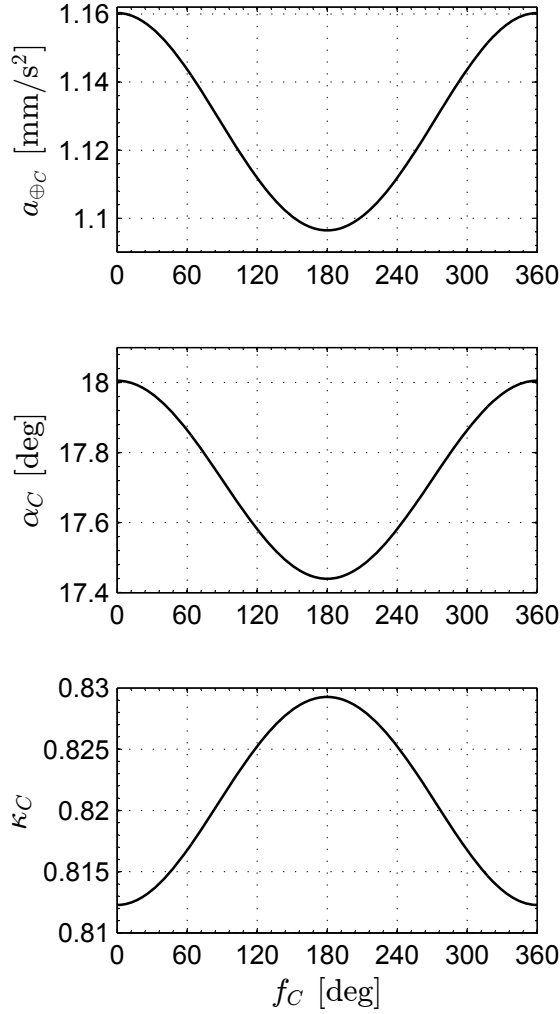
Figure 4: Performance requirements for the chief spacecraft along an Earth-synchronized PFDO with $a_C = 0.95\,\text{au}$ and $H_C = 0.05\,\text{au}$.

The deputies are assumed to track a general circular orbit (GCO) [1] with a radius of $100\,\text{km}$ relative to the chief spacecraft. The parametric representation of the desired GCO for the i-th deputy, in the chief's rotating reference frame $\mathcal{T}_R$, has the following algebraic form

$$[\boldsymbol{\rho}_i^\star]_{\mathcal{T}_R} = \begin{bmatrix} \rho_{i_x}^\star \\ \rho_{i_y}^\star \\ \rho_{i_z}^\star \end{bmatrix} = \begin{bmatrix} 50 \sin\left[n_r\, t + \dfrac{(i-1)\,\pi}{3}\right] \\ 100 \cos\left[n_r\, t + \dfrac{(i-1)\,\pi}{3}\right] \\ 50\sqrt{3} \sin\left[n_r\, t + \dfrac{(i-1)\,\pi}{3}\right] \end{bmatrix}\ \text{km} \tag{36}$$

where n_r is the desired angular velocity of the given relative orbit. In the following simulations, the period of the relative orbit is assumed to be equal to that of the Earth (the reference celestial body of this scenario), that is, $n_r = \sqrt{\mu_\odot/r_\oplus^3}$.

4.1. Undirected topology graph

Consider first an undirected and connected topology. To evaluate the performance of the controller defined in Eq. (24), introduce the error index $\boldsymbol{e}_{ij} \triangleq \boldsymbol{q}_i - \boldsymbol{q}_j$ and $\dot{\boldsymbol{e}}_{ij} \triangleq \dot{\boldsymbol{q}}_i - \dot{\boldsymbol{q}}_j$, with initial values reported

11

in Tab. 1.

	$e_{ij} \cdot \hat{x}_R$ [km]	$e_{ij} \cdot \hat{y}_R$ [km]	$e_{ij} \cdot \hat{z}_R$ [km]	$\dot{e}_{ij} \cdot \hat{x}_R$ [m/s]	$\dot{e}_{ij} \cdot \hat{y}_R$ [m/s]	$\dot{e}_{ij} \cdot \hat{z}_R$ [m/s]
$i=1, j=2$	2.5	-1	0	1.8×10^{-4}	-1.3×10^{-4}	-9×10^{-5}
$i=1, j=3$	-1	-3.5	3	1.2×10^{-4}	-1.1×10^{-4}	-9×10^{-5}
$i=2, j=3$	-3.5	-2.5	3	-6×10^{-5}	2×10^{-5}	0

Table 1: Initial errors of deputy E-sails in the undirected case.

The communication topology that describes the information flow of the three E-sail-based deputies is illustrated in Fig. 5, and the weighted adjacency matrix $\mathcal{W}$ is

$$\mathcal{W} = \begin{bmatrix} 0 & 1 & 2 \\ 1 & 0 & 2 \\ 2 & 2 & 0 \end{bmatrix} \tag{37}$$

The feedback gain K_i in Eq. (24) is chosen as $K_i = I_3$ and, after a trial and error procedure, the dimensionless parameters for a fast convergence rate are assumed to be $\xi = 10^5$ and $\zeta = 5 \times 10^{-3}$.
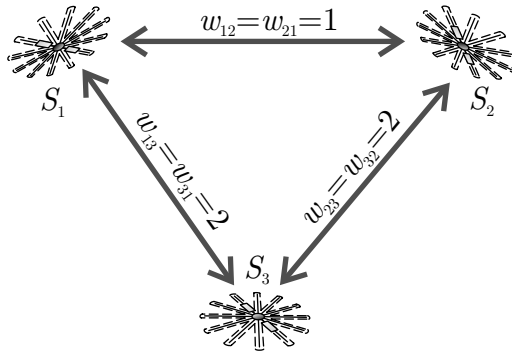
Figure 5: Undirected topology of the three deputy E-sails.

The position and velocity errors of the three deputies are shown in Fig. 6 and Fig. 7 respectively, while the time variations of the (relative) control variables $\Delta \varphi_i$, $\Delta \theta_i$ and $\Delta \beta_i$ are shown in Fig. 8. Note that with the control law given by Eq. (24), all errors converge to zero and consensus is reached within two days. Moreover, the final consensus guarantees a similar transfer time of all deputies, which is important for practical purposes as it reduces the maneuver time of the whole formation.

As is indicated by **Theorem 1**, the connectivity of the information exchange topology is a requisite for formation consensus. To illustrate this point, another two typical formation structures are analyzed here whose communication topologies are give in Fig. 9. Assuming the initial errors are given by Tab. 1, the position and velocity errors with the topologies shown in Fig. 9(a) are illustrated in Fig. 10 and Fig. 11, while the errors in case (b) are shown in Fig. 12 and Fig. 13. Note that in case (a), although no direct path exists between S_1 and S_3, the information flow of S_1 and S_3 can still be passed through S_2. Therefore, the corresponding topology graph is connected and consensus can be achieved. By comparison, the position errors of the formation system with a communication topology given by Fig. 9(b) are not convergent, due to the fact that S_3 is isolated and the topology graph is unconnected.

4.2. Directed topology graph

The second case illustrates the performance of the consensus algorithm in a directed information exchange topology. The initial conditions of the three deputies are now slightly different from the reference trajectories, see Eq. (36), and the initial errors are reported in Tab. 2.
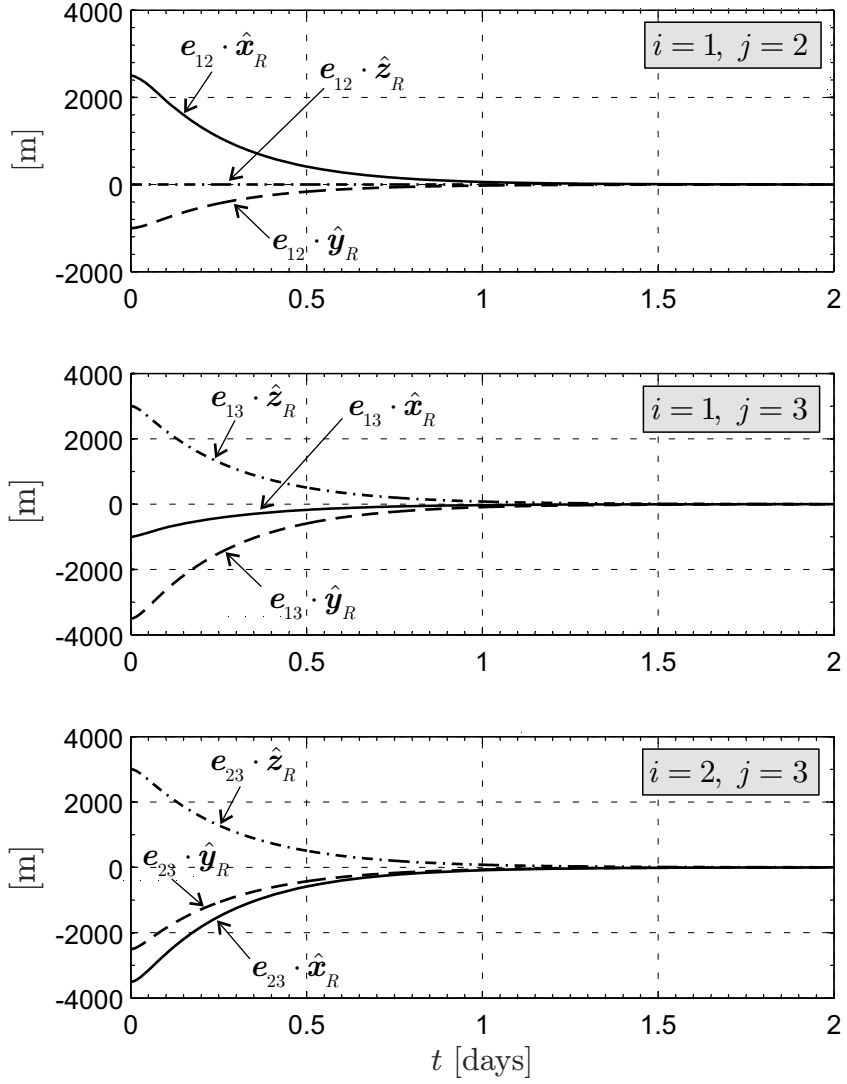
12

Figure 6: Time variation of position errors $\boldsymbol{e}_{ij}$ using an undirected topology graph.

	$\boldsymbol{e} \cdot \hat{\boldsymbol{x}}_R$ [km]	$\boldsymbol{e} \cdot \hat{\boldsymbol{y}}_R$ [km]	$\boldsymbol{e} \cdot \hat{\boldsymbol{z}}_R$ [km]	$\dot{\boldsymbol{e}} \cdot \hat{\boldsymbol{x}}_R$ [m/s]	$\dot{\boldsymbol{e}} \cdot \hat{\boldsymbol{y}}_R$ [m/s]	$\dot{\boldsymbol{e}} \cdot \hat{\boldsymbol{z}}_R$ [m/s]
S_1	1	-1	0.5	3×10^{-5}	-5×10^{-5}	4×10^{-5}
S_2	-0.5	1	-1	-3×10^{-5}	5×10^{-5}	-4×10^{-5}
S_3	-1	-0.5	1	5×10^{-5}	-4×10^{-5}	-3×10^{-5}

Table 2: Initial errors of deputy E-sails in the directed case.

The communication graph of the three deputy spacecraft is shown in Fig. (14), while the (asymmetric) weighted adjacency matrix $\mathcal{W}$ is

$$\mathcal{W} = \begin{bmatrix} 0 & 1 & 2 \\ 1 & 0 & 0 \\ 0 & 2 & 0 \end{bmatrix} \tag{38}$$

The controller performance is governed by the parameters σ and ζ. Assume that a pair $\{\sigma, \zeta\}$ has been
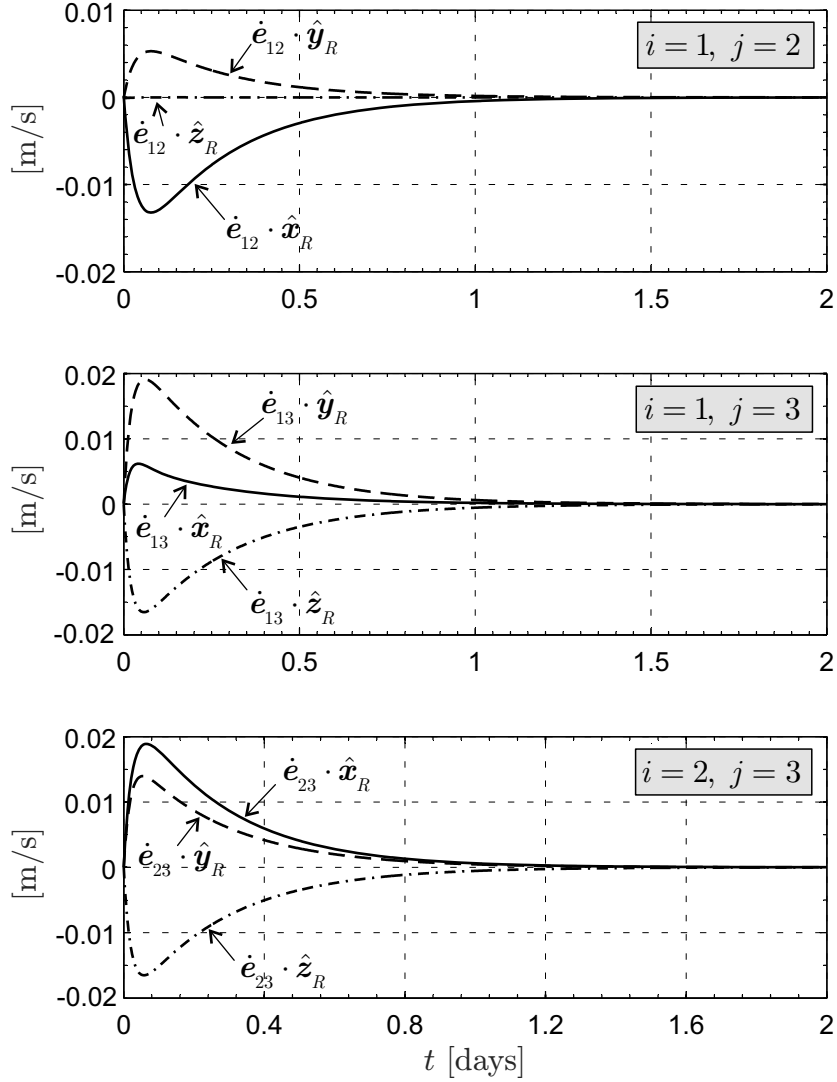
Figure 7: Time variation of velocity errors $\dot{\boldsymbol{e}}_{ij}$ using an undirected topology graph.

chosen. To obtain a faster convergence, σ should be increased and ζ decreased. In doing so, the cost to be paid is of a lower transition accuracy and a higher control input. Assuming $\sigma = 10^5$, the eigenvalues of $-(\sigma\, I_N + \mathcal{L})$ are found to be $\lambda_{1,2,3} \simeq 10^5$. When these values are substituted into Eq. (35), the constraint to be met is $\zeta > 4.47 \times 10^{-3}$. In the simulations ζ is therefore chosen equal to 5×10^{-3}, in order to obtain an asymptotic stability and a good convergence rate.

To illustrate the effectiveness of the control law (30), the variations of relative position errors $\boldsymbol{e}_i$ and relative velocity errors $\dot{\boldsymbol{e}}_i$ are plotted in Figs. 15-16 for a time interval of two days. The figures show that the transient errors of the three deputy E-sails gradually converge to zero after about one day. The corresponding time histories of control variables $\Delta\,\varphi_i$, $\Delta\,\theta_i$ and $\Delta\,\beta_i$ are shown in Fig. 17.

Unlike the undirected case, the control law of Eq. (30) does not require the topology to be connected. For illustration, the information exchange topology is assumed unconnected and is given by Fig. 18. The relative position and velocity errors presented in Fig. 19 and Fig. 20 clearly show that although S_3 is isolated from S_1 and S_2, consensus can still be reached while the final errors all converge to zero.

14
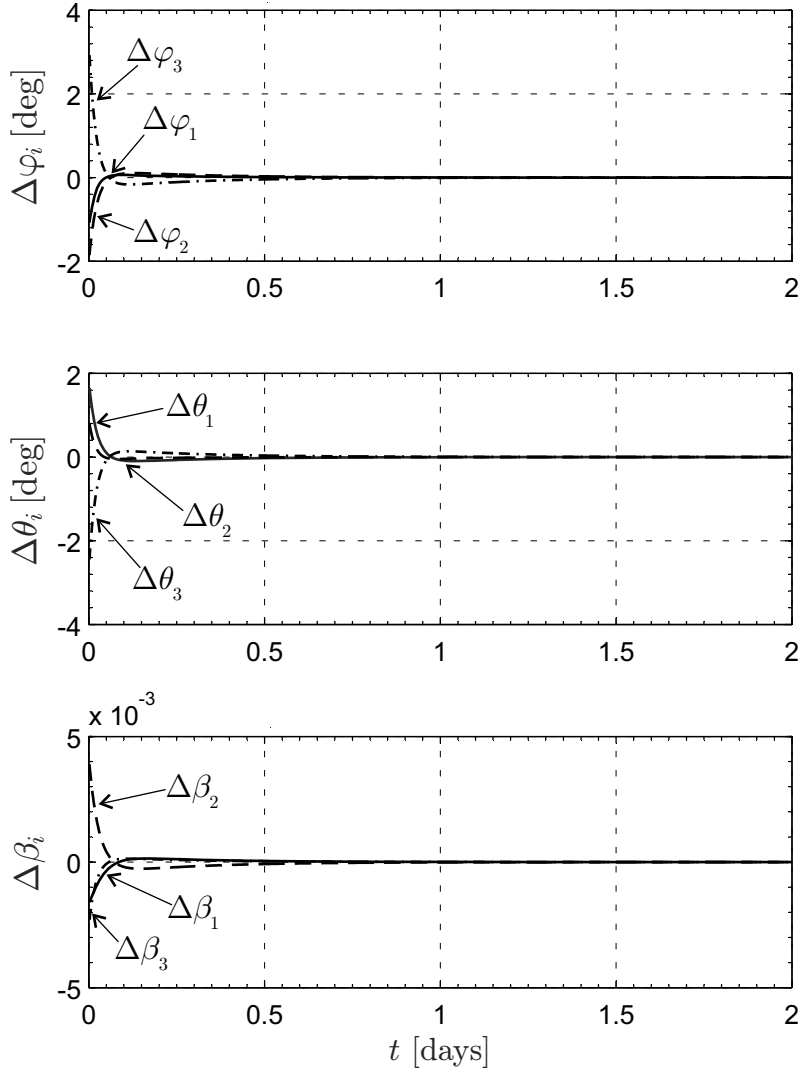
Figure 8: Time variation of the control input using an undirected topology graph, see Eq. (24).

5. Conclusions

The problem of E-sail formation flying around a heliocentric elliptic displaced orbit tracked by a chief has been investigated. The chief-deputy relative motion has been described in the chief rotating reference frame. Distributed architectures of the formation control system, which accommodate a single E-sail-based chief and a number of deputies, have been proposed for both the undirected and directed case. The maintenance of the formation flying relies on the proposed consensus algorithms that are, in essence, protocols formulated on information exchange topologies with information link couplings.

Illustrative examples have shown that, using the information available from the neighbours, the presented distributed cooperative control laws enable each vehicle to reach the final consensus. Compared to a classical chief-deputy approach, the introduction of deputy-to-deputy information coupling guarantees a time-balanced formation control during the transient motion. The control algorithm remains effective even in case of limited or faulty communication links within the formation, thus enhancing the robustness and redundancy of the whole system.

15
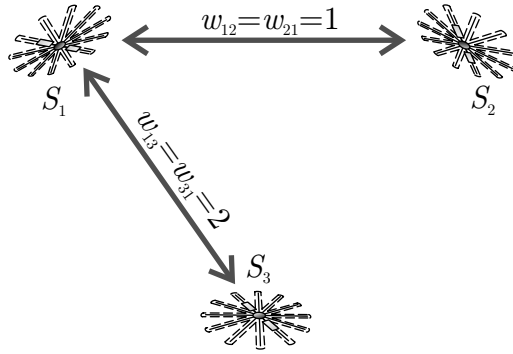
(a) S_3 partially connected.
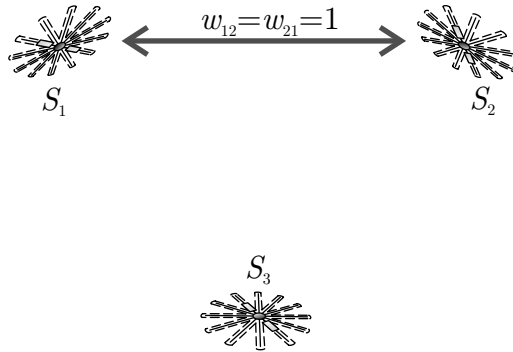
(b) S_3 isolated.

Figure 9: Two typical communication topologies.

6. Acknowledgements

References

[1] Alfriend, K., Vadali, S. R., Gurfil, P., How, J., Breger, L., Spacecraft formation flying: Dynamics, control and navigation. Elsevier, Oxford, Ch. 5, pp. 84–90, 2010.

[2] Balch, T., Arkin, R. C., Behavior-based formation control for multirobot teams. IEEE transactions on robotics and automation 14 (6), 926–939, doi: 10.1002/rnc.1147, 1998.

[3] Gong, S., Baoyin, H., Li, J., Solar sail formation flying around displaced solar orbits. Journal of Guidance, Control, and Dynamics 30 (4), 1148–1152, doi: 10.2514/1.24315, July-August 2007.

[4] Gong, S., Gao, Y., Li, J., Solar sail formation flying on an inclined earth orbit. Acta Astronautica 68 (1-2), 226–239, doi: 10.1016/j.actaastro.2010.08.022, January-February 2011.

[5] Gong, S., Li, J., Solar sail heliocentric elliptic displaced orbits. Journal of Guidance, Control, and Dynamics 37 (6), 2021–2025, doi: 10.2514/1.G000660, November 2014.

[6] Janhunen, P., Increased electric sail thrust through removal of trapped shielding electrons by orbit chaotisation due to spacecraft body. Annales Geophysicae 27 (8), 3089–3100, doi: 10.5194/angeo-27-3089-2009, August 2009.

[7] Janhunen, P., Sandroos, A., Simulation study of solar wind push on a charged wire: basis of solar wind electric sail propulsion. Annales Geophysicae 25 (3), 755–767, doi: 10.5194/angeo-25-755-2007, March 2007.

[8] Mazal, L., Gurfil, P., Cluster flight algorithms for disaggregated satellites. Journal of Guidance, Control, and Dynamics 36 (1), 124–135, doi: 10.2514/1.57180, January-February 2013.

[9] McInnes, C. R., The existence and stability of families of displaced two-body orbits. Celestial Mechanics and Dynamical Astronomy 67 (2), 167–180, doi: 10.1023/A:1008280609889, February 1997.

[10] Mengali, G., Quarta, A. A., Janhunen, P., Electric sail performance analysis. Journal of Spacecraft and Rockets 45 (1), 122–129, doi: 10.2514/1.31769, January-February 2008.
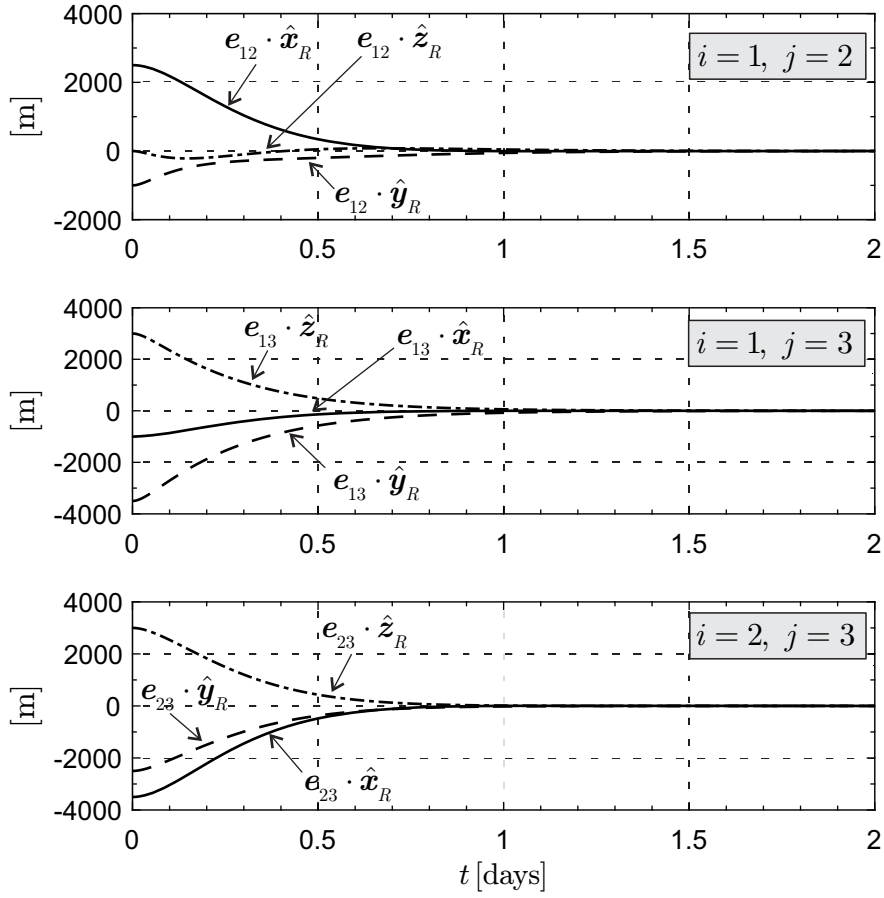
Figure 10: Time variation of position errors e_{ij} with a communication topology of Fig. 9(a).

[11] Niccolai, L., Quarta, A. A., Mengali, G., Electric sail elliptic displaced orbits with advanced thrust model. Acta Astronautica In press., doi: 10.1016/j.actaastro.2016.10.036, 2016.

[12] Ren, W., Consensus based formation control strategies for multi-vehicle systems. In: American Control Conference. IEEE, Minneapolis, Minnesota (USA), pp. 4237–4242, 14–16 June 2006.

[13] Ren, W., Formation keeping and attitude alignment for multiple spacecraft through local interactions. Journal of Guidance, Control, and Dynamics 30 (2), 633–638, doi: 10.2514/1.25629, March–April 2007.

[14] Ren, W., Distributed leaderless consensus algorithms for networked Euler-Lagrange systems. International Journal of Control 82 (11), 2137–2149, doi: 10.1080/00207170902948027, November 2009.

[15] Ren, W., Atkins, E., Distributed multi-vehicle coordinated control via local information exchange. International Journal of Robust and Nonlinear Control 17 (11), 1002–1033, doi: 10.1002/rnc.1147, 2007.

[16] Salazar, F., McInnes, C., Winter, O., Intervening in earth's climate system through space-based solar reflectors. Advances in Space Research 58 (1), 17–29, doi: 10.1016/j.asr.2016.04.007, July 2016.

[17] Salazar, F., Winter, O., Macau, E., Masdemont, J., Gómez, G., Zero drift regions and control strategies to keep satellite in formation around triangular libration point in the restricted sun-earth-moon scenario. Advances in Space Research 56 (7), 1502–1518, doi: 10.1016/j.asr.2015.07.001, October 2015.

[18] Sanchez-Torres, A., Drag and propulsive forces in electric sails with negative polarity. Advances in Space Research 57 (4), 1065–1071, doi: 10.1016/j.asr.2015.12.013, February 2016.

[19] Slotine, J. E., Li, W., Applied nonlinear control. NJ: Prentice-Hall, New York, pp. 124–128, 1991.

[20] Spielman, D., 2012. Spectral graph theory. In: Naumann, U., Schenk, O. (Eds.), Combinatorial Scientific Computing. Chapman and Hall/CRC, Ch. 18, pp. 495–500.

[21] Toivanen, P., Janhunen, P., Envall, J., Merikallio, S., Electric solar wind sail control and navigation. Advances in the Astronautical Sciences 145, 275–285 , 2012.

[22] Toivanen, P. K., Janhunen, P., Spin plane control and thrust vectoring of electric solar wind sail. Journal of Propulsion and Power 29 (1), 178–185, doi: 10.2514/1.B34330, January-February 2013.

[23] Wang, W., Mengali, G., Quarta, A. A., Yuan, J., Extreme values of relative distances for spacecraft in elliptic displaced orbits. Advances in Space Research 58 (4), 475–487, doi: 10.1016/j.asr.2016.05.007, August 2016.

[24] Wang, W., Mengali, G., Quarta, A. A., Yuan, J., Formation flying for electric sails in displaced orbits. Part I: Geometrical
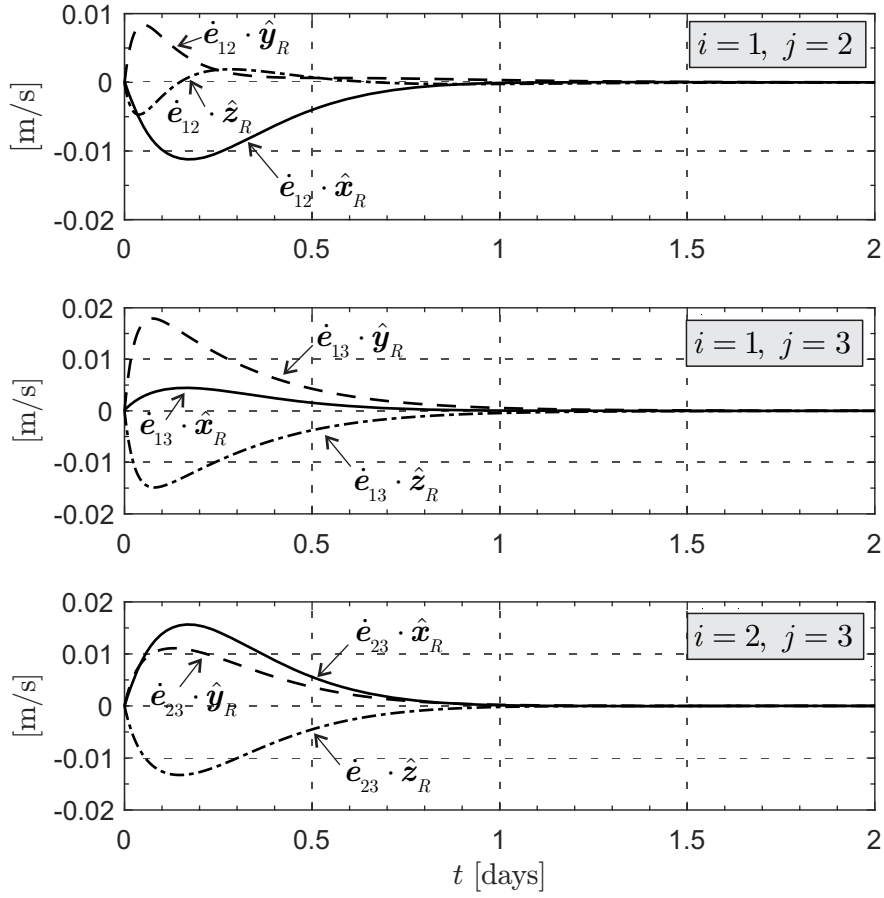
Figure 11: Time variation of velocity errors $\dot{\boldsymbol{e}}_{ij}$ with a communication topology of Fig. 9(a).

analysis. Advances in Space Research (submitted) , 2017.

[25] Wang, W., Yuan, J., Mengali, G., Quarta, A. A., Invariant manifold and bounds of relative motion between heliocentric displaced orbits. Journal of Guidance, Control and Dynamics 39 (8), 1764–1776, doi: 10.2514/1.G001751, August 2016.

[26] Yamaguchi, K., Yamakawa, H., Study on orbital maneuvers of electric sail with on-off thrust control. Aerospace Technology Japan 12, 79–88, doi: 10.2322/astj.12.79, 2013.

[27] Yamaguchi, K., Yamakawa, H., Electric solar wind sail kinetic energy impactor for asteroid deflection missions. The Journal of the Astronautical Sciences 63 (1), 1–22, doi: 10.1007/s40295-015-0081-x, March 2016.
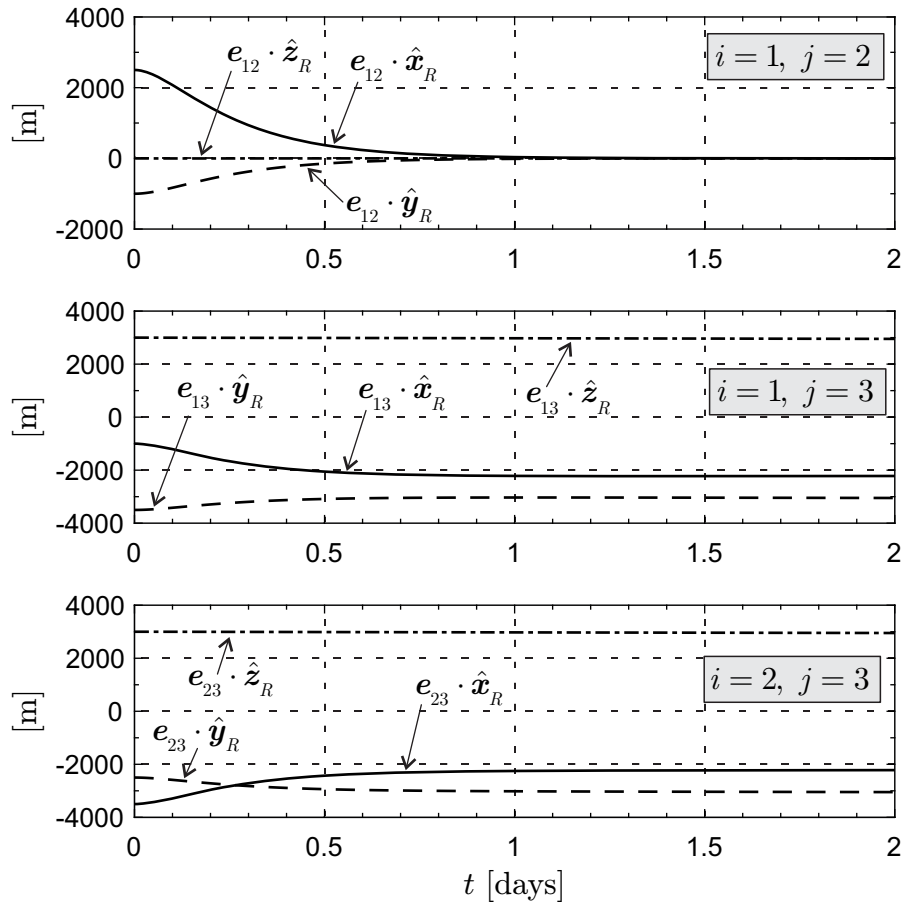
Figure 12: Time variation of position errors $\boldsymbol{e}_{ij}$ with a communication topology of Fig. 9(b).

19
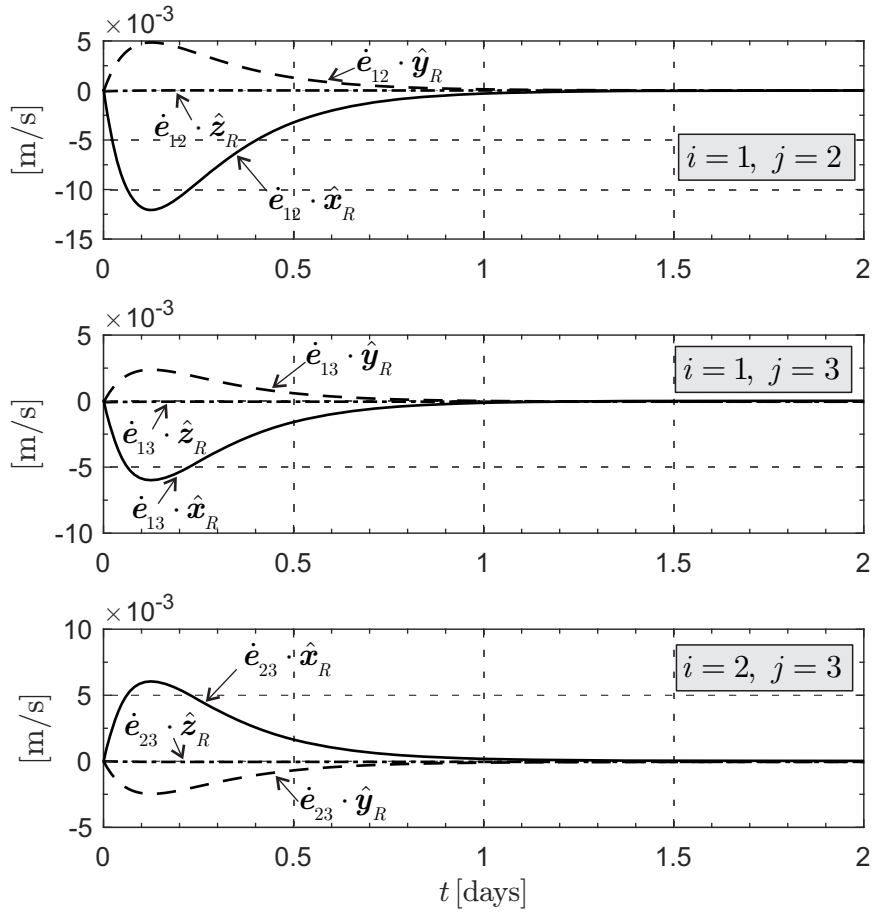
Figure 13: Time variation of velocity errors $\dot{\boldsymbol{e}}_{ij}$ with a communication topology of Fig. 9(b).
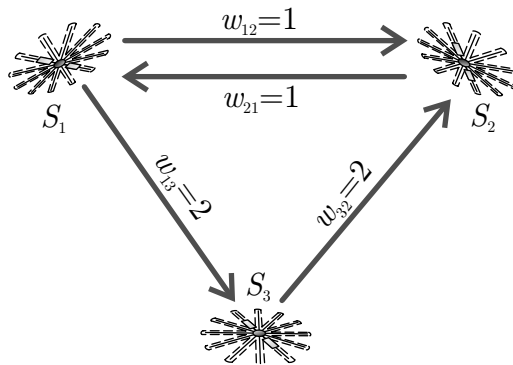
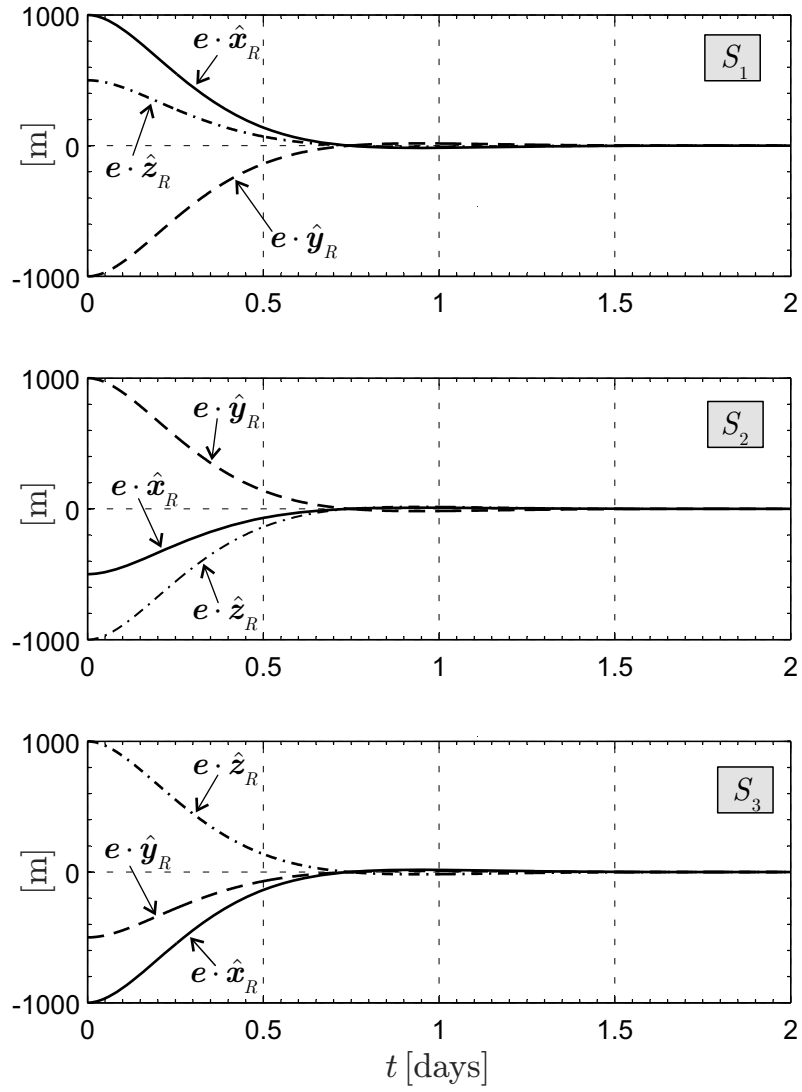
Figure 14: Directed topology of the three deputy sails.

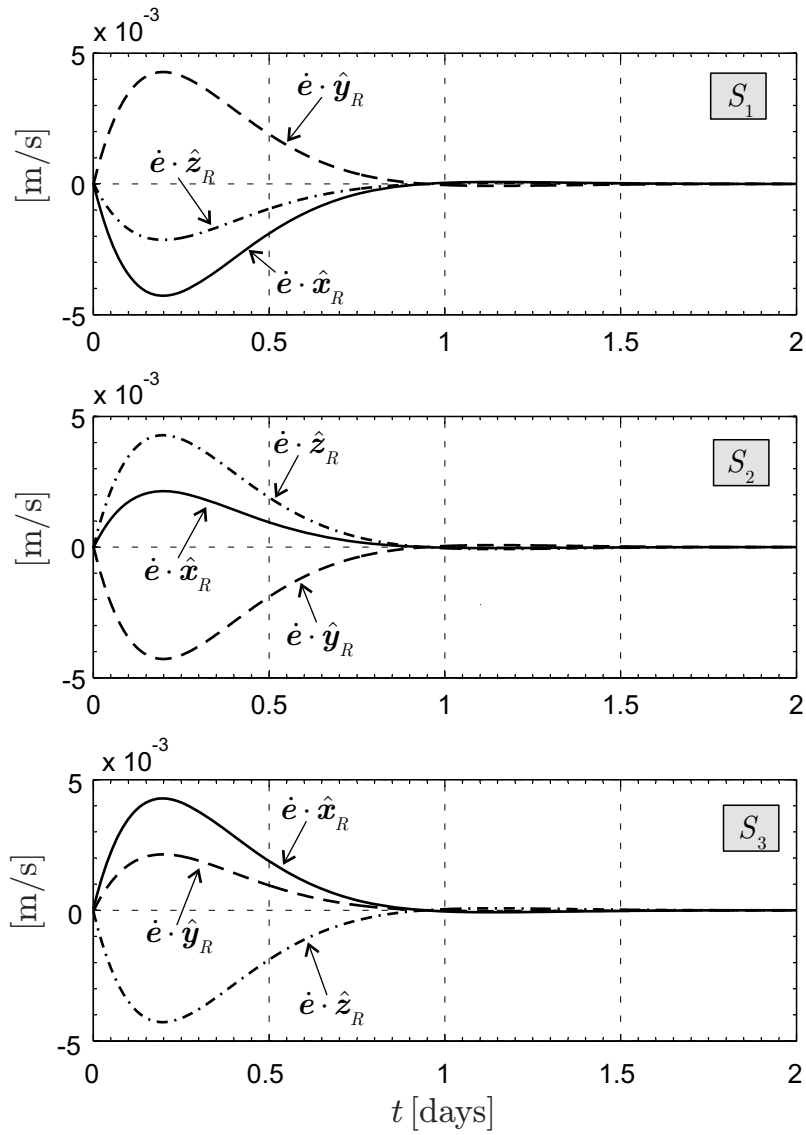Figure 15: Time variation of position errors using a directed topology graph.

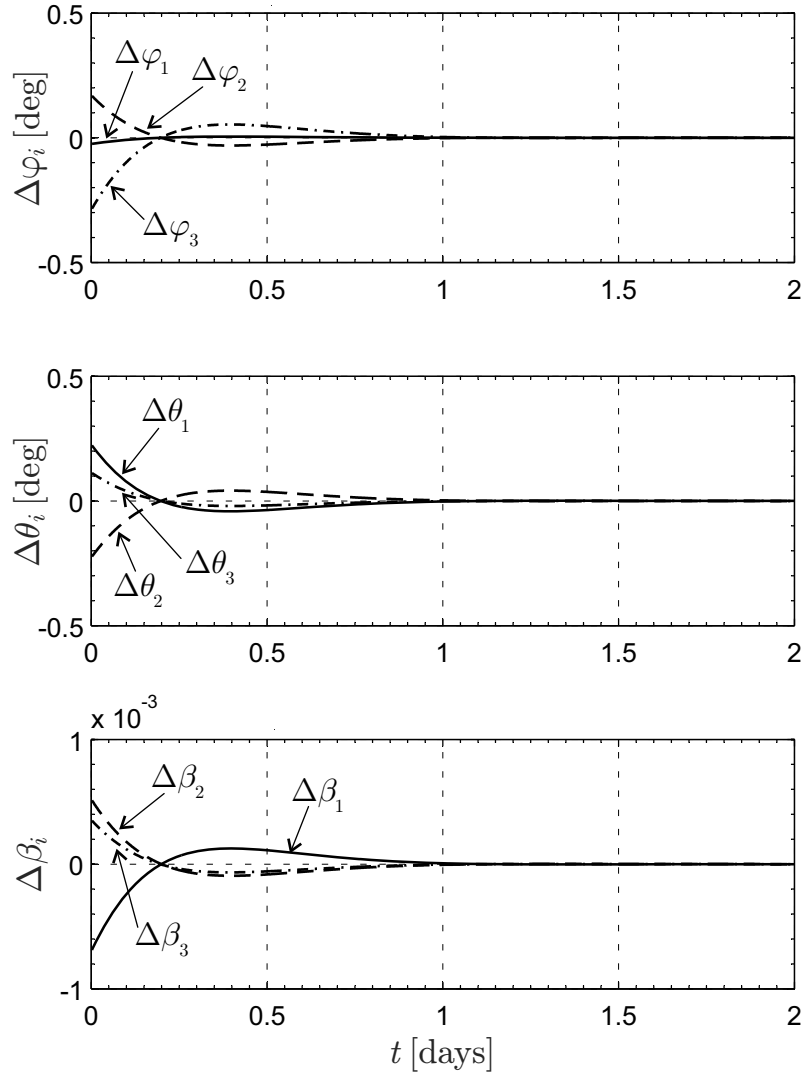Figure 16: Time variation of velocity errors using a directed topology graph.

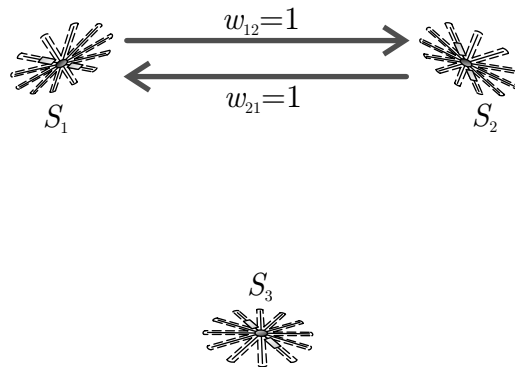Figure 17: Time variation of control input $\boldsymbol{u}_i$ using a directed topology graph, see Eq. (30).

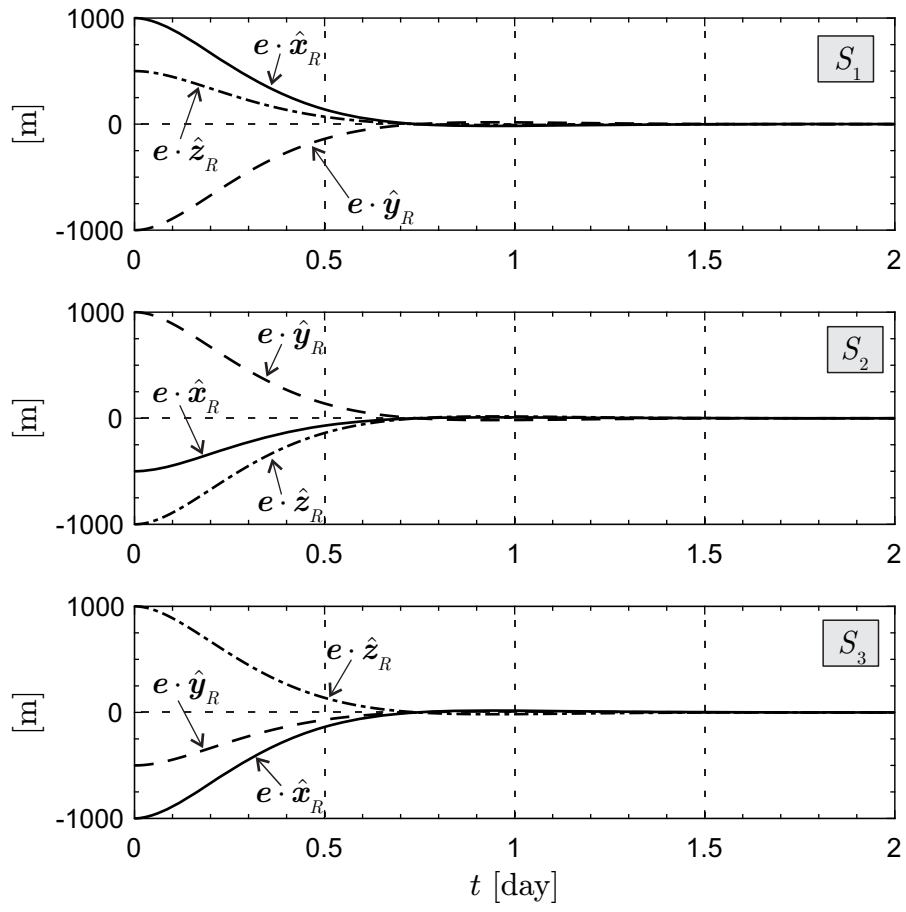Figure 18: Unconnected directed topology of the three deputy sails.

23

Figure 19: Time variation of position errors when the unconnected directed topology is given by Fig. 18.
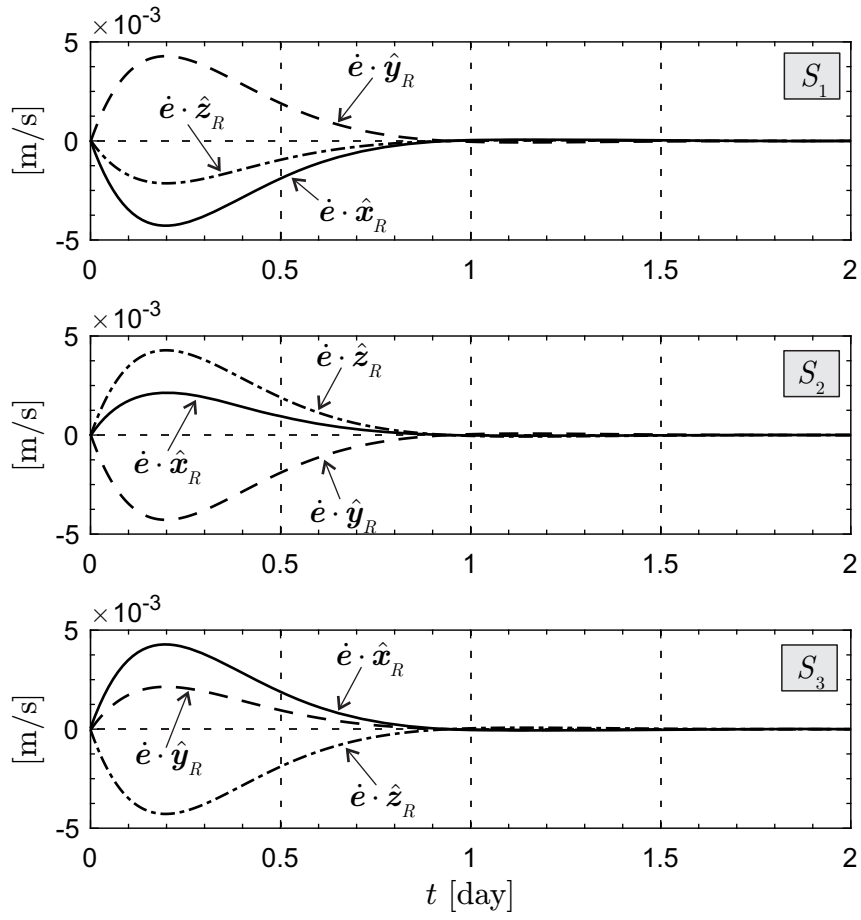
24

Figure 20: Time variation of velocity errors when the unconnected directed topology is given by Fig. 18.